PHYSICAL REVIEW A, VOLUME 65, 043807

Mode locking in Fabry-Perot semiconductor lasers

Yoshinori Nomura,* Seiji Ochi, Nobuyuki Tomita, Koichi Akiyama, and Toshiro Isu
Advanced Technology R & D Center, Mitsubishi Electric Corporation 1-1, Tsukaguchi-Honmachi 8-Chome, Amagasaki, Hyogo 661-8661, Japan

Tohru Takiguchi and Hideyo Higuchi†
HF & Optical Semiconductor Division, Mitsubishi Electric Corporation 4-1, Mizuhara, Itami, Hyogo 664-8641, Japan
(Received 29 May 2001; published 21 March 2002)

Passive mode-locking (ML) operation in semiconductor quantum-well (QW) lasers with Fabry-Perot (FP) cavities is investigated theoretically and experimentally. Structural and operational conditions for a semiconductor QW laser to exhibit ''amplitude modulation (AM)'' or ''frequency modulation'' ML operations are investigated by numerical analysis based on a semiclassical laser model. It is shown experimentally that clear AM ML pulses self-build and persist under continuous current injection in $In_{1-x}Ga_xAs/In_{1-x}Ga_xAs_yP_{1-y}/InP$-based FP QW lasers with cavity lengths of 300-600 μm. The observed ML features are explained in terms of the laser model.

DOI: 10.1103/PhysRevA.65.043807 PACS number(s): 42.55.Px, 42.60.Fc

I. INTRODUCTION

Mode locking (ML) in multimode laser operations is a well-known phenomenon where mode separations near each other and relative phases between oscillating modes are fixed so that beat notes (or periodic pulses) are emitted from the laser. The pulse separation corresponds to the time it takes for an optical pulse to complete one round trip in the cavity. There are engineering interests in the ML of semiconductor lasers, because an ML laser can emit very short optical pulses with almost ideal time-bandwidth products and high repetition rates. Thus, there are potential applications for high-bit-rate optical-communication systems [1].

It is widely recognized that a saturable-absorber (SA) region as well as a gain region should be placed in the cavity to get stable ML in a semiconductor laser [1–4]. In such a configuration, ML is supposed to rely on a short net-gain window that only supports an optical pulse and discriminates from the noise that might grow outside of the pulse. In much of the literature, such passive ML phenomena are analyzed in the time domain: the action on the mode-locked pulse within the laser cavity by components, such as a gain and SA, is analyzed, and the net modification of the pulse upon return to the starting reference plane is set equal to zero [5]. An SA seems to be an indispensable ingredient for the steady-state operation of ML semiconductor lasers.

On the other hand, the semiclassical laser theory, in which the optical field is analyzed in the frequency domain, predicts steady-state ML's of multimode lasers regardless of whether they are with or without any SA [6,7]. The criteria for a multimode laser to operate with ML have been derived for two-level laser media [6]. In the theory, mechanisms for both equalizing the mode separations and steadying optical and atomic states invoke third-order nonlinear interactions of optical fields with gain media. This argument is readily extended to a semiconductor laser by modeling the semiconductor gain medium as an ensemble of noninteracting two-level systems [8]. However, it is still an open question as to whether and when a multimode semiconductor laser (without any SA) can yield stable ML pulses. First, because semiconductor media are highly dispersive and have wide gain spectra, the ML conditions are rather intricate. Second, there are few experimental investigations of semiconductor-laser ML that parallel with the theory, although transient beat notes have been observed from GaAs-based Fabry-Perot (FP) semiconductor lasers [9,10].

In this paper, addressing this question, we present numerical results that demonstrate that a multimode-quantum well (QW) laser with an FP cavity exhibits ''amplitude modulation (AM)'' or ''frequency modulation (FM)'' ML [11], depending on the mode-frequency separation, the length of gain region along the cavity axis, and the amounts of linear and nonlinear chromatic dispersions of the gain region. We also report on experimental results using $In_{1-x}Ga_xAs/In_{1-x}Ga_xAs_yP_{1-y}/InP$-based FP QW lasers with emission wavelengths in a 1.55-μm band with cavity lengths ranging from 200 to 600 μm [12]. It is shown that clear AM ML pulses self-build and persist under continuous current injection in lasers with cavity lengths of 300–600 μm. High extinction ratios reaching up to 10 dB and almost Fourier-transform-limited time-bandwidth products of the optical pulses reveal that all modes are coupled with each other and generate pulses as the superposition of the modal fields.

Section II is divided into two parts. We briefly summarize essential equations and approximations used to model FP semiconductor lasers in Sec. II A. The formulation consists of coupled-mode equations for amplitudes and phases and rate equations for carrier densities in a QW. The equations related to optical fields are derived from the self-consistency equations [6]. (An explicit expression for the optical-dipole-matrix element is given in Appendix B.) The rate equations are derived from a Liouville equation for the density matrix

*Email address: nomura.yoshinori@wrc.melco.co.jp
†Present address: Osaka Electro-Communication University, 18-8 Hatsu-Cho, Neyagawa, Osaka 572-8530, Japan.

 ©2002 The American Physical Society

of a free electron in the QW [13], where the semiconductor medium is assumed to consist of quasitwo-dimensional (2D) free electrons and holes in quasiequilibrium. The derivation is summarized in Appendix A. The excitation process of the QW is modeled by balance equations for 3D carrier densities with drift-diffusion currents that are solved together with Poisson's equation for the electrical potential in the semiconductor medium. In the excitation process, a trapping time from the 3D to 2D electronic states and escape time for the reverse process are assumed. Simultaneous solutions of all the equations fully define the optical and electronic states of the laser. In particular, spectra of the phase differences among modes reveal whether the laser is operating in AM or FM ML. We present systematic numerical solutions of the equations in Sec. II B. Section III presents details and results of the experimental investigations of the AM ML in multiple-QW semiconductor lasers. A discussion and summary in Sec. IV conclude the paper.

II. NUMERICAL ANALYSIS

A. Model

1. Coupled mode equations

In order to model FP lasers, we use coupled-mode equations for amplitudes and phases. We consider transverse electric (TE) modes only because most semiconductor lasers oscillate selectively in TE modes. The scalar electric field can be expanded by the normal modes of the FP cavity,

$$\mathcal{E}(y,z,t)=\frac{1}{2}\sum_{n} E_n(t)\exp\{-\imath(\nu_n t+\phi_n)\}Y_n(y)Z_n(z)+\text{c.c.}$$

Here, ν_n is the frequency of the nth mode and E_n and ϕ_n are the nth-mode amplitude and phase, respectively. The function $Z_n(z)$ $(=\sin\beta_n z)$ is the nth longitudinal mode. We include the transversal field-distribution function of the nth mode, $Y_n(y)$, to scale the coupling between the optical field and semiconductor media QW's. We assume that the waveguide holds a single transversal mode only and is homogeneous along the x direction of coordinates.

Under the slowly varying amplitude approximation and the rotating-wave approximation, we obtain coupled-mode equations for the amplitudes and phases [14],

$$\frac{\partial E_n^2}{\partial t}=2(a_n-b_n)E_n^2-2\sum_{\mu}\sum_{\rho}\sum_{\sigma} E_nE_\mu E_\rho E_\sigma \times\text{Im}\{\vartheta_{n\mu\rho\sigma}\exp(\imath\Psi_{n\mu\rho\sigma})\}+\zeta_n n_{2D}, \tag{1}$$

$$\nu_n+\frac{\partial\phi_n}{\partial t}=\Omega_n+\sigma_n-\sum_{\mu}\sum_{\rho}\sum_{\sigma} E_\mu E_\rho E_\sigma E_n^{-1} \times\text{Re}\{\vartheta_{n\mu\rho\sigma}\exp(\imath\Psi_{n\mu\rho\sigma})\}. \tag{2}$$

Here, $\Psi_{n\mu\rho\sigma}$'s are relative phase angles,

$$\Psi_{n\mu\rho\sigma}=(\nu_n-\nu_\mu+\nu_\rho-\nu_\sigma)t+\phi_n-\phi_\mu+\phi_\rho-\phi_\sigma .$$

These angles are assumed to be very slowly varying, and hence only the mode indices that follow the relation

$$n=\mu-\rho+\sigma$$

are taken into account, Ω_n is the cavity frequency defined by $\Omega_n=cK_n$, where $K_n^2\equiv-(1/Y_n)(d^2Y_n/dy^2)+\beta_n^2$ and c is the speed of light. b_n denotes optical losses due to the round-trip loss and free-carrier absorption. The linear gain a_n and mode shift σ_n are, respectively, the imaginary and real part of the optical linear response and, with perfect $\mathbf{k}$ conservation, read

$$\sigma_n+\imath a_n=\frac{\imath\nu_n S_{nn}^y S_{nn}^z}{2\varepsilon_0\hbar V}\sum_{\mathbf{k}} \mathcal{N}_{\mathbf{k}}|d_{cv\mathbf{k}}|^2\mathcal{D}(\omega_{\mathbf{k}}-\nu_n), \tag{3}$$

where V is the volume of the gain region, ε_0 is the permitivity of the vacuum, $\hbar$ is the Planck constant divided by 2π, $\mathcal{N}_{\mathbf{k}}$ is the population inversion given by Fermi-Dirac distribution functions for electrons in the conduction band and holes in the valence band (see Appendix A for an explicit expression), $d_{cv\mathbf{k}}$ is the electric-dipole element between the electronic states (Appendix B), $\mathcal{D}(\Delta\omega)$ is a complex Lorentzian defined by $\mathcal{D}(\Delta\omega)\equiv1/(\gamma+\imath\Delta\omega)$ with the dephasing rate γ [see Eq. (A4)], and $\omega_{\mathbf{k}}$ is the angular frequency of light accompanied by the electron transition. The summation runs over all $\mathbf{k}$ vectors in the first Brillouin zone and the conduction and valence bands. The geometric figure of the gain region is defined by $\mathcal{N}_{\mathbf{k}}(y)=\mathcal{N}_{\mathbf{k}}S^y(y)S^z(z)$ with $S^y(y)=1$ and $S^z(z)=1$ in QW's and $S^y(y)=0$ and $S^z(z)=0$ elsewhere. The confinement factor S_{nn}^y is defined by $S_{nn}^y=\int_{-\infty}^{\infty}Y_n^2S^y(y)dy/\int_{-\infty}^{\infty}Y_n^2dy$ and $S_{nn}^z=\int_0^L Z_n^2S^z(z)dz/\int_0^L Z_n^2dz$, where L is the cavity length. Coupling coefficients $\vartheta_{n\mu\rho\sigma}$ due to third-order polarization are given by

$$\vartheta_{n\mu\rho\sigma}=\frac{\imath\nu}{64\hbar^3\varepsilon_0V}S_{n\mu\rho\sigma}^yS_{n\mu\rho\sigma}^z\{\mathcal{D}_c(\nu_\rho-\nu_\sigma)+\mathcal{D}_v(\nu_\rho-\nu_\sigma)\} \times\sum_{\mathbf{k}} \mathcal{N}_{\mathbf{k}}(d_{cv\mathbf{k}})^4\mathcal{D}(\omega_{\mathbf{k}}-\nu_\mu+\nu_\rho-\nu_\sigma) \times\{\mathcal{D}(\omega_{\mathbf{k}}-\nu_\sigma)+\mathcal{D}^*(\omega_{\mathbf{k}}-\nu_\rho)\}, \tag{4}$$

where

$$S_{n\mu\rho\sigma}^y=\int_{-\infty}^{\infty}Y_nY_\mu Y_\rho Y_\sigma S^y(y)dy\Big/\int_{-\infty}^{\infty}Y_n^2dy$$

and

$$S_{n\mu\rho\sigma}^z=\int_0^L[1+\cos\{2(\beta_\sigma-\beta_\rho)z\} +\cos\{2(\beta_\mu-\beta_\rho)z\}]S^z(z)dz\Big/\int_0^L Z_n^2dz. \tag{5}$$

$\mathcal{D}_x(\Delta\omega)$ are again complex Lorentzian's, defined by $\mathcal{D}_x(\Delta\omega)\equiv1/(\gamma_x+\imath\Delta\omega)$, where γ_x $(x=c$ or $v)$ is the decay

rate of free carriers in the conduction band or valence band. The decay rate is dominated by the spontaneous emission rate in the QW. In Eq. (1), we added the term $\zeta_n n_{2D}$ phenomenologically to take into account spontaneous emissions that couple to the modal amplitude. This term is necessary for the onset of lasing.

2. Pumping process

Equations (1) and (2) should be consistent with the electronic state in the QW, whose dynamics is described by the rate equation for 2D carrier density n_{2D},

$$\frac{\partial n_{2D}}{\partial t}=\Xi_c-\gamma_c n_{2D}-\sum_n c_n E_n^2, \tag{6}$$

where $c_n=\varepsilon_0 a_n/\hbar \nu_n \Gamma_n$. Here, $\Gamma_n=(\int_{-\infty}^{\infty}S^y dy \int_0^L S^z dz)/(\int_{-\infty}^{\infty}Y_n^2 dy\int_0^L Z_n^2 dz)$. Equation (6) is derived by spatially averaging the equations of motion for the diagonal element of the density matrix (Appendix A). In Eq. (6), Ξ_c is the averaged pumping rate. The value of Ξ_c is given as a parameter in conventional calculations. Therefore, in usual treatments, the charge neutrality and flat-potential profile around the active region are assumed. However, both the potential profile and carrier distribution determine the actual electronic system and, as described later, the stabilities of these variables are required as a ML condition. Therefore, we adopt here a more realistic pumping model, where we treat the 3D carrier transport by the balance equation

$$\frac{\partial n_{3D}}{\partial t}+\mathrm{div}J^c=-G-\Xi_c, \tag{7}$$

where G represents thermal relaxations of free carriers and J^c is the current density, which is described by the drift-diffusion model,

$$J^c=-n_{3D}\ \mu^c \mathrm{grad}(-\Phi+V^c)-D^c \mathrm{grad}\ n_{3D}. \tag{8}$$

Here, μ^c is the electron mobility, V^c is the band discontinuity in the conduction-band edge, and D^c is the diffusion coefficient of 3D electrons. The parameter Ξ_c couples Eq. (6) with Eq. (7) and is assumed here to have the form

$$\Xi_c=-n_{2D}/\tau_{escape}+n_{3D}/\tau_{trap}, \tag{9}$$

where τ_{escape} is the time for 2D electrons to escape from the 2D states to the 3D states and τ_{trap} is the time for the reverse process. Similar equations for holes corresponding to Eqs. (6)–(9) can be derived and are used for calculations. The potential Φ in Eq. (8) and all the charge distributions should satisfy Poisson's equation,

$$\mathrm{div}(\varepsilon\,\mathrm{grad}\Phi)=-\varrho, \tag{10}$$

where ε denotes the permittivity and ϱ is the charge distribution that includes ionized-impurity distributions and free-carrier distributions.

Equations (1), (2), (6), (7), and (10) and the corresponding equations for holes model FP semiconductor lasers and may have solutions when boundary conditions, that is, static applied voltages between the electrodes of the diode are given.

3. Mode-locking conditions

Mode-locking conditions are derived from the dynamics of phases, Eq. (2) [6]. For the sake of simplicity, we consider a three-mode operation and label these modes as 1, 2, and 3 in ascending-frequency order. From Eq. (2), we obtain the ML equation by

$$\frac{\partial \Psi}{\partial t}=d+l_s \sin\Psi+l_c\cos\Psi, \tag{11}$$

where the relative phase Ψ is

$$\Psi\equiv\Psi_{2123}=(2\nu_2-\nu_1-\nu_3)t+2\phi_2-\phi_1-\phi_3, \tag{12}$$

detuning d is

$$d=2\sigma_2-\sigma_1-\sigma_3-\sum_{m=1}^{3}(2\tau_{2m}-\tau_{1m}-\tau_{3m})E_m^2, \tag{13}$$

with $\tau_{nm}=\mathrm{Re}(\vartheta_{nnmm}+\vartheta_{nmmn})$, and the ML coefficients l_s, l_c are

$$l_s=\mathrm{Im}\left\{2E_1E_3(\vartheta_{2123}+\vartheta_{2321})+\left(\frac{\vartheta_{1232}E_3}{E_1}+\frac{\vartheta_{3212}E_1}{E_3}\right)E_2^2\right\}, \tag{14}$$

$$l_c=\mathrm{Re}\left\{-2E_1E_3(\vartheta_{2123}+\vartheta_{2321})+\left(\frac{\vartheta_{1232}E_3}{E_1}+\frac{\vartheta_{3212}E_1}{E_3}\right)E_2^2\right\}. \tag{15}$$

Equation (11) can be rewritten as

$$\frac{\partial\Psi}{\partial t}=d+l\sin(\Psi+\Psi_0), \tag{16}$$

where

$$l=\sqrt{l_s^2+l_c^2}$$

and

$$\Psi_0=\tan^{-1}(l_c/l_s).$$

ML occurs when

$$\frac{\partial\Psi}{\partial t}=0, \tag{17}$$

for which the inequality relation

$$|d|<l \tag{18}$$

TABLE I. Material parameters of the laser model.

	p-clad	p-SCH	p-SCH	QW	n-SCH	n-SCH	n-clad
Thickness (nm)	100	60	30	5.3	30	60	100
Arsenic fraction y	0	0.31		1	0.31		0
Donor density (10^{18} cm^3)		0.05			0.1	0.5	1
Acceptor density (10^{18} cm^3)	1	0.5	0.3		0.2	0.1	0.0

must be satisfied, because all the quantities in Eq. (16) should be real. The linear stability of solutions $\Psi^{(s)}$ of Eq. (17) can be examined by the usual procedure and is attained provided

$$\cos(\Psi^{(s)}+\Psi_0)<0. \quad (19)$$

If a solution $\Psi^{(s)}$ is obtained for Eq. (17), which satisfies the relation (19), ML will arise and continue.

Once a stable solution, which has the form

$$\Psi^{(s)}=\sin^{-1}(-d/l)-\tan^{-1}(l_c/l_s) \quad (20)$$

is obtained, it leads by definition [Eq. (12)] to the equation

$$(\nu_2-\nu_1)t+\phi_2-\phi_1=(\nu_3-\nu_2)t+\phi_3-\phi_2+\Psi^{(s)}. \quad (21)$$

Equation (21) should hold regardless of time t. Thus $\nu_2-\nu_1=\nu_3-\nu_2$ and then Eq. (21) is reduced to

$$\phi_2-\phi_1=\phi_3-\phi_2+\Psi^{(s)}. \quad (22)$$

Equation (22) indicates that $\Psi^{(s)}$ is the residual phase difference of one from the other two modes. $\Psi^{(s)}$ characterizes the ML pulse built from the three modes. If $-\pi/2<\Psi^{(s)}<\pi/2$, then all three modes oscillate almost in-phase and high ML pulses will be obtained. Otherwise, if $\pi/2<\Psi^{(s)}<3\pi/2$, then one of the three modes oscillates out of phase. If we look at the energy region where $d\rightarrow 0$, the condition $-\pi/2<\Psi^{(s)}<\pi/2$ is equivalent to $l_s<0$ and the condition $\pi/2<\Psi^{(s)}<3\pi/2$ is equivalent to $l_s>0$, which was claimed by Sargent *et al.* [6]. However, as shown later, $\Psi^{(s)}$ often has a wide spectral width crossing over $\pm\pi/2$ for semiconductor lasers. Therefore, to study the ML feature of semiconductor lasers, we should know the $\Psi^{(s)}$ spectrum precisely.

In order to obtain the $\Psi^{(s)}$, we shall solve the set of equations that describe FP semiconductor lasers, as described above; the coupled amplitude and phase equations, Eqs. (1) and (2) for $n=1$, 2, and 3 with equations modeling the pumping of carriers, that is, Poisson's Equation (10), the rate equation (6) for 2D electrons, the balance equation (7) for 3D electrons, and the corresponding equations for holes.

ML conditions (17) and (19) state, however, only that mode separations have the same value and the residual phase difference is fixed to a constant value under ML. Under the ML condition, however, we may, further, expect that the oscillating frequency itself will be fixed. This situation will occur if the time derivatives of optical and electrical variables vanish. Thus, we shall solve the set of equations in steady states.

B. Results of calculations

We seek steady-state solutions of the set of equations, solving numerically by iteration [15]. We consider the spatial dependence of variables in a one-dimensional coordinate, i.e., the y direction only.

The structural and material parameters of the reference laser model used in calculations are listed in Table I. The laser has a separate confinement heterostructure (SCH). The active layer is a single QW with separate confinement layers on both sides and the outermost layers are InP cladding layers. All these layers are composed of $In_{1-x}Ga_xAs_yP_{1-y}$/InP layers lattice matched to the InP substrate. We postulate that the *n*-cladding layer contacts with an electron bath made of the same material as the cladding layer. Similarly, the hole bath is put on the *p*-cladding layer. In calculations, the bath layers are supposed to serve as carrier reservoirs. In other words, the bath layers are not only in thermal equilibrium in themselves, but also the quasi-Fermi energies in the layers are fixed by the applied voltage.

When we calculate for multiple QW's instead of the single QW, we expediently multiply the number of wells to confinement factors S^y_{nn} and $S^y_{n\mu\rho\sigma}$ in Eqs. (3), (4), and (6) and the well width in the rate equation (6) so as to scale the coupling between optical fields and the electronic system. This implies that all the QW's act as an identical QW being injected with the same amount of carriers and interacting with the same optical field. Throughout this paper, we concentrate on the case of eight QW's that prove to exhibit a clear ML.

The parameters, such as band-gap energies and effective electron and hole masses of materials, are calculated using the empirical equations given by Agrawal and Dutta [16]. The dephasing rate γ is assumed to have a constant value of 30 ps^{-1} [17]. The spontaneous-emission rate γ_c, which should be equal to γ_v, is calculated by $\gamma_c=B\sqrt{n_{2D}p_{2D}}$, where B is a spontaneous-emission coefficient and has value 0.04 nm^3/ps [18]. Trapping time τ_{trap} may be close to the intraband relaxation rate and is taken to be 0.1 ps. τ_{escape} is assumed to be 0.167 ps for electrons and 0.128 ps for holes. All these trapping times are chosen so that the center frequencies of laser oscillations, which are experimentally obtained for 300- to 600-μm-cavity lasers, can be reproduced by calculations within an appropriate bias-voltage region, 0.8–1.2 V. The internal loss is taken to be 20 cm^{-1}, which is experimentally determined. The mirror loss is estimated by $\ln(1/R^2)/2L$, where the facet reflectivity R is 0.3. The electron mobility $\mu^c=3000$ cm^2/V s, and hole mobility $\mu^v=124$ cm^2/V s, are used in the balance equations for 3D carriers. The carrier temperature is assumed to be 300 K. The

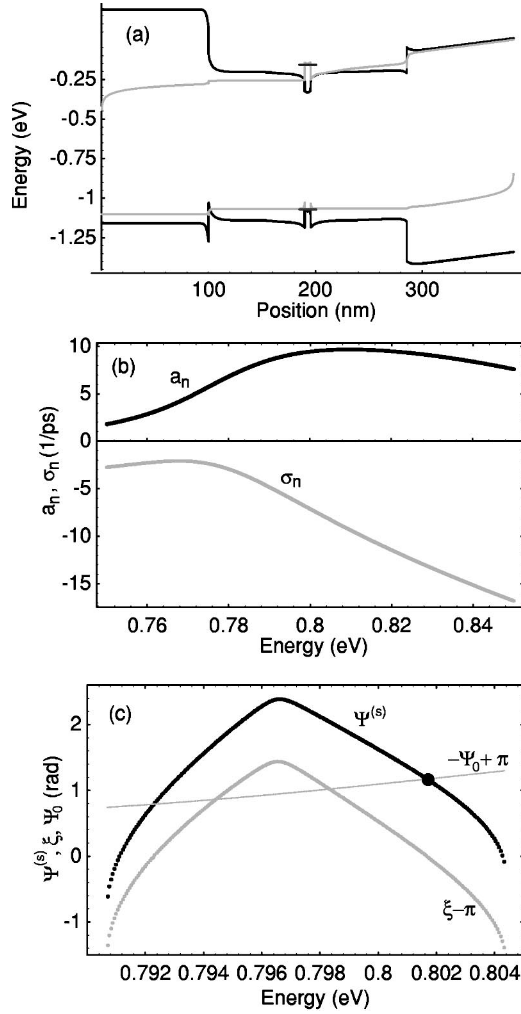

FIG. 1. Calculated results for a 300-μm-cavity laser when a 1.1 V is applied. (a) is for the conduction- and valence-band edges together with quasi-Fermi energies pertaining to the respective bands. (b) is for the spectra of the linear gain a_n and the mode-frequency shift σ_n. (c) is for the spectra of Ψ^s, ξ, and Ψ_0.

activation energies of donors and acceptors are, respectively, 6 and 23 meV.

First, we look at the calculated results for the set of equations, as an example, for a 300-μm cavity laser at an applied voltage of 1.1 V. Figure 1(a) shows the conduction- and valence-band-edge profiles together with quasi-Fermi energies that pertain to the respective bands. Quasi-Fermi energies for 2D carriers are indicated by bars. It is noticeable that the quasi-Fermi energy for free electrons in the QW is high compared to that in the SCH layer. The geometric mean of carrier densities of electrons and holes in the QW is 5.27×10^{18} cm^{-3} in this case. The free-electron accumulations in QW's are commonly observed in the calculated results described below. The apparent electron accumulation in the QW is caused by the potential profile that forms the QW: that is, holes are trapped and hardly escape from the QW because of their small mobility and high band discontinuity at the well-barrier interface. Thus, holes accumulate in the QW first, then free electrons accumulate in the QW to compensate for the excess space charge. The high quasi-Fermi energy in the conduction band may result in a wide gain spectrum and favors multimode operation of the laser.

Figure 1(b) shows the spectra of the linear gain a_n and mode frequency shift σ_n. The gain spectrum is wide compared to the mode separation: i.e., about 0.58 meV. An almost but not exactly linear dispersion curve of the mode-frequency shift σ_n in the high-gain spectral region can be seen.

We obtained the steady-state solution at the energy for the center mode with the phase difference $\Psi^{(s)}$, as marked by a filled circle (●) in Fig. 1(c). The amplitudes obtained are 2.62, 2.65, and 2.68 kV/m for the three modes in ascending-energy order. The spectra for $\xi=\sin^{-1}(-d/l)$, Ψ_0, and $\Psi^{(s)}=\xi-\Psi_0$ shown in Fig. 1(c) are calculated by the so-called "decoupled approximation" [6], in which the electronic state and amplitudes in the laser are assumed to be the same as the solutions. The curve $\Psi^{(s)}$ means that all modes falling into the spectral range can exhibit mode-locked oscillations with the corresponding residual phase difference $\Psi^{(s)}$. The spectral curve of $\Psi^{(s)}$ represents the ML state of the oscillating laser.

We next see $\Psi^{(s)}$ curves for cavity lengths of 300, 600, and 1100 μm changing applied voltages from 0.8 to 1.2 V with an increment of 0.05 V. The solutions obtained are shown in Fig. 2. Figure 2(a) shows the calculated spectra of $\Psi^{(s)}$ for applied voltages 0.95, 1.0, 1.05, 1.1, and 1.15 V in a 300-μm-cavity laser. For each applied voltage, the mark corresponds to the center-mode energy $\hbar\nu_2$ obtained as the steady-state solution of the set of equations. Carrier densities are, from the lower applied voltage, 5.18, 5.23, 5.25, 5.27, and 5.28 in units of 10^{18} cm^{-3}. As the applied voltage is increased, the oscillating frequency of the center mode and spectral ML range shift toward higher frequencies because of the band-filling effect and the change of the potential profile. The values of $\Psi^{(s)}$ are lower than $\pi/2$ and, hence, a clear AM ML may occur for the 300-μm-cavity laser.

The amplitudes and phases of modes that lie out of the spectral range vary in time because the ML condition, Eq. (17), is not satisfied, and amplitudes E_n and frequency ν_n include the frequency component of $\partial\Psi/\partial t$. Therefore, mode frequencies no longer separate with even intervals and mode intensities will include noise at around the frequency of $\partial\Psi/\partial t$.

For the 300-μm cavity laser, there is no stable solution for applied voltages lower than 0.9 V that satisfies condition (18) and Eq. (17). This is because modal intensities required for condition (18) are not attained due to gain shortage. Therefore, again, the amplitudes and phases will vary in time.

There is no stable solution for the 300-μm-cavity laser for the applied voltage of 1.2 V even though condition (18) is satisfied. For this case, the modal intensity and center frequency fluctuate in a time scale of hundreds of picoseconds. At this and presumably higher excitation levels, the linear-stabilization condition is no longer adequate.

The calculated spectrum of $\Psi^{(s)}$ for stable ML changes appreciably for longer cavity lasers. Figure 2(b) shows the calculated spectra of $\Psi^{(s)}$ in a 600-μm-cavity laser for applied voltages of 0.9 (5.12), 0.95 (5.22), 1.0 (5.25), 1.05 (5.27), 1.1 (5.29), 1.15 (5.32), and 1.2 (5.35) V. Hereafter, we

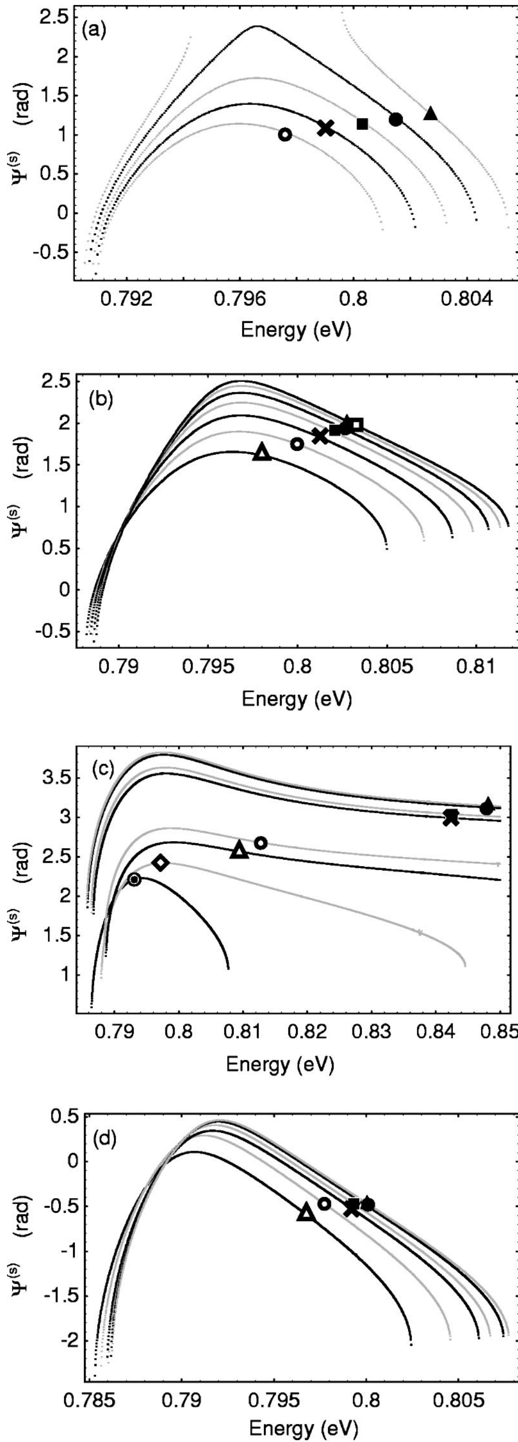

FIG. 2. Calculated spectra of $\Psi^{(s)}$ for various applied voltages in FP lasers with cavity lengths of (a) 300,(b) 600, and (c) 1100 μm. For case (d), the cavity length is 1100 μm but the excitation region is restricted to a half part of the middle of the cavity. The marks attached to the curves indicate $\Psi^{(s)}$'s and energies at which steady-state solutions are obtained for the applied voltages. The marks denote applied voltages; from the low voltage, the sun mark is for 0.8, diamond for 0.85, open triangle for 0.9, open circle for 0.95, cross for 1.0, filled square for 1.05, disk for 1.1, triangle for 1.15, and open square 1.2 V. The corresponding carrier densities obtained by the calculations are given in the text.

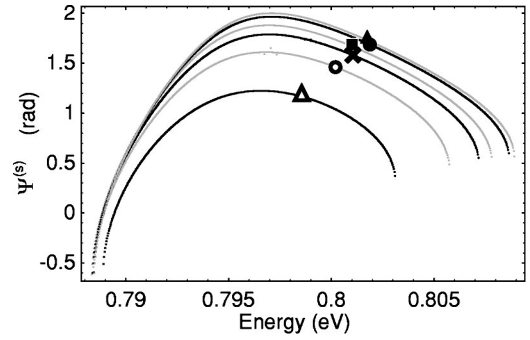

FIG. 3. Calculated spectra of $\Psi^{(s)}$ for a 600-μm-cavity laser with a well width of 6 nm. Other parameters are given in Table I. The spectra are obtained for applied voltages of 0.9–1.15 V with an increment of 0.05 V. The marks have the same meanings as in Fig. 2

write in the parentheses following the applied voltages the carrier densities in units of 10^{18} cm^{-3} that are obtained as results of the calculations. Figure 2(b) reveals that $\Psi^{(s)}$ increases and becomes greater than $\pi/2$ as the applied voltage increases. Thus, the laser will eventually exhibit FM ML.

If the cavity length is 1100 μm, $\Psi^{(s)}$ becomes greater than $\pi/2$, as shown in Fig. 2(c), and the laser will exhibit FM ML in the whole range of the applied voltage. The applied voltages (and carrier densities) are 0.8 (4.10), 0.85 (4.98), 0.9 (5.08), 0.95 (5.17), 1.0 (5.22),1.05 (5.24), 1.1 (5.25), and 1.15 (5.27) V (10^{18} cm^{-3}).

For engineering purposes, it may be worthy to note that $\Psi^{(s)}$'s for 1100-μm lasers can be remarkably reduced by restricting the excitation region to the middle of the cavity. Figure 2(d) shows the calculated spectra of $\Psi^{(s)}$ for the device structure of a 1100-μm cavity, in which the excitation region is restricted to a half part of the middle of the cavity. The applied voltages and carrier densities obtained as solutions for the curves in Fig. 2(d) are 0.9 (5.09), 0.95 (5.17), 1.0 (5.23), 1.05 (5.25), 1.1 (5.26), and 1.15 (5.28) V (10^{18} cm^{-3}).

To see the effects of well width on the ML state, after changing the well width from 5.3 nm to 6 nm, we solve the equations for a 600-μm-cavity laser for applied voltages of 0.8 to 1.2 V with an increment of 0.05 V. Steady-state solutions are obtained for voltages (carrier densities) of 0.9 (5.02), 0.95 (5.12), 1.0 (5.18), 1.05 (5.22), 1.1 (5.23), and 1.15 (5.24) V (10^{18} cm^{-3}). The results are shown in Fig. 3. Comparing Fig. 3 with Fig. 2(b), we see that $\Psi^{(s)}$ can be reduced slightly by widening the well width.

III. EXPERIMENTAL RESULTS

In this section, we demonstrate actual device operations. We made FP semiconductor lasers by a three-step growth using metal-organic vapor phase epitaxy on an n-type InP substrate. The active region consists of eight QW's of $In_{0.53}Ga_{0.47}$ As separated by 10-nm-thick barriers of $In_{1-x}Ga_xAs_yP_{1-y}$($\lambda_g = 1.325$ μm) and 80-nm separate confinement layers with the same constituent as that of barriers. The QW width was chosen so that the photoluminescence spectrum peaked at 1.55 μm wavelength. After mesa-

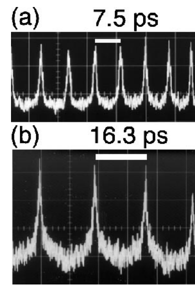

FIG. 4. Autocorrelation traces for lasers with cavity lengths (a) 300 and (b) 600 μm.

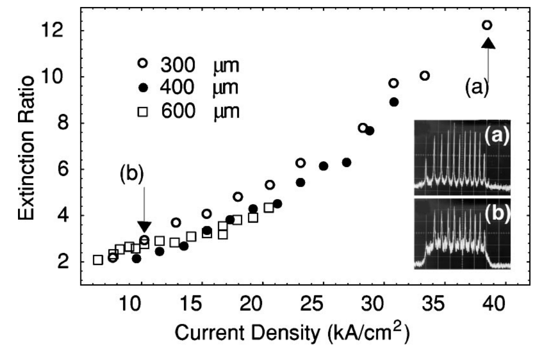

FIG. 5. Extinction ratios plotted against injection current densities for lasers with cavity lengths 300, 400, and 600 μm. Depicted are autocorrelation traces from the laser with the 300–μm-cavity length. Traces are shown within a window in a time domain outside of which is shown the noise level as the reference for extinction ratios. Each of the traces corresponds to the point indicated by (a) and (b) in the plot.

etching, which formed the waveguide, Fe-doped semi-insulating InP layers were grown for current blocking. The lateral width of the gain region is 1.3 μm. Cladding layers are S-doped and Zn-doped (10^{18} cm^{-3}) InP layers. A highly Zn-doped $In_{1-x}Ga_xAs$ layer was grown on the top and served as the contact. The cavity lengths of prepared lasers are 200, 300, 400, and 600 μm. As-cleaved facets are used as the cavity mirrors. The threshold currents of the lasers at room temperature ($25°C$) are 8.6, 7.8, 8.6, and 10.4 mA in order of the cavity length.

ML pulses were observed by autocorrelation through second-harmonic generation (SHG) with a time resolution of 0.1 ps using a $LiIO_3$ crystal at room temperature. The spectra of emitted light from the lasers were measured by the optical-spectrum analyzer with a spectral resolution of 0.05 or 0.1 nm.

A semiconductor laser connected with a 45 Ω resistor in series was driven by a continuous or pulse current with 8 ns duration and 2 μs period. The current density was estimated from the applied voltage, impedance, and laser geometry. The output light was led by a single-mode fiber to an Er-doped optical-fiber amplifier where the light was amplified by 15 dB. Then the light was led to the autocorrelator.

In Fig. 4, autocorrelation traces are shown for lasers with cavity lengths (a) 300 and (b) 600 μm driven by pulse currents of densities 41 and 20.5 kA/cm^2, respectively. The pulse separation of each trace is (a) 7.5 ps and (b) 16.3 ps corresponding to the round-trip time for a pulse in the cavity. This fact indicates that the pulses are caused by beats between adjacent modes, i.e., ML. We observed similar ML pulses from a 400-μm-cavity laser, while signals of ML pulses from a 200-μm cavity laser were almost at noise level. We observed clear ML pulses, when the 300-μm-cavity laser was driven by continuous currents. In order to avoid heating up the lasers, we hereafter carried out experiments using pulse currents.

In Fig. 5, extinction ratios are plotted against injection-current densities for lasers with cavity lengths of 300, 400, and 600 μm. Extinction ratios for all samples tend to increase when the injection-current density is increased. The tendency can be explained by the broadening of the ML spectral region due to the band filling and increase of mode amplitudes. If the number of modes are increased, the extinction ratio of the optical pulse becomes larger because the pulse is constructed by the superposition of the modal fields. The highest applied voltage available was limited by the pulse generator's capability.

The relations between pulse widths in the time domain and spectral widths when the 300-μm-length laser is driven by current densities of 20.5 kA/cm^2 and 41 kA/cm^2 are shown in Fig. 6. Assuming a sech^2 function as the shape of the optical pulses in the time domain, we estimate the pulse widths as (a) 0.41 ps and (b) 0.31 ps. The spectral widths for the respective current densities are (c) 0.86 ps^{-1} and (d) 1.38 ps^{-1}. The time-bandwidth products are 0.35 and 0.41 for 20.5 kA/cm^2 and 41 kA/cm^2, respectively. The values are very close to the ideal transform-limited value 0.35. The fact that the pulse width decreases when the spectral width broadens shows that all modes shown in Fig. 6 correlate with each other in phase.

It would be necessary to examine the effects of optical amplification on mode-locked pulses. When the input power is raised, the gain spectrum of the amplifier is deformed: the gain around the 1540 nm wavelength distinctly declines compared to the other wavelength region due to gain saturation. Because the specific devices investigated above have oscillating modes in the spectral hole-burning region, pulses may have been deformed by the amplification. To evaluate

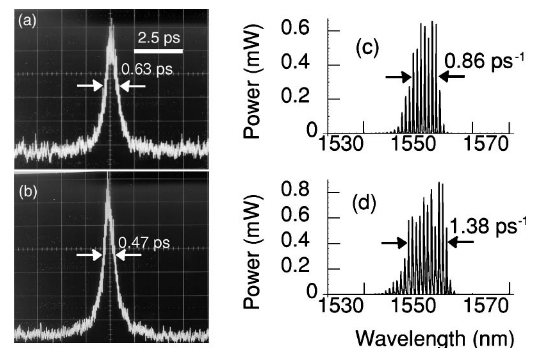

FIG. 6. Relations between pulse widths in the time domain and spectral widths when the 300–μm-length laser is driven by current densities 20.5 kA/cm^2 [(a) and (c)] and 41 kA/cm^2 [(b) and (d)].

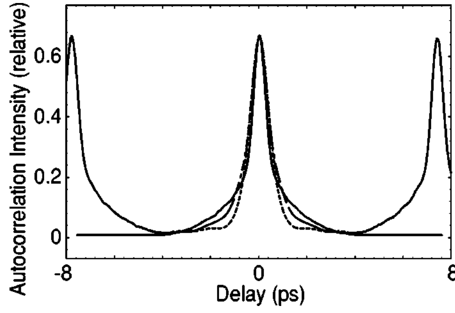

FIG. 7. The autocorrelation trace (solid curve) of ML pulses from the 300–μm-cavity laser and calculated autocorrelation traces from the power spectra of the laser light (dashed curve) and amplified laser light (dot dashed curve). The laser is driven by a current density of 41 kA/cm^2.

the effects of the nonlinearity of the amplification on the mode-locked pulses, we calculate the autocorrelations of the pulses, which are reconstructed by Fourier transformation from the power spectra of mode-locked pulses after and before amplification, and compare the autocorrelation traces with those by SHG. The results are shown in Fig. 7 for the 300-μm-cavity laser driven by a current density of 41 kA/cm^2. Figure 7 shows that the foot part of the pulse is widened after the amplification. This may reflect the dynamics of the gain saturation and recovery of the Er^+-doped fiber amplifier. The "pedestal" of the SHG autocorrelation trace is wider than the calculated autocorrelations. This reveals that chromatic dispersion of the amplifier affects the pulse shape in addition to the effects due to the spectral hole burning. However, as far as the pulse width at half maximum is concerned, only a small change by the amplification is appreciable.

IV. DISCUSSION AND SUMMARY

We investigated passive ML of semiconductor lasers. A semiclassical laser model with a free-carrier approximation was used for modeling semiconductor QW lasers. The pumping process was modeled so that the carrier transfer and potential profile in a one-dimensional coordinate are taken into account. Steady-state solutions were obtained for a three-mode operation. We used the material parameters given in the literature except for two escape times from the 2D to 3D states for free electrons and holes, with values chosen so that the lasing spectra obtained experimentally can be reproduced by calculations with appropriate applied voltages.

We verified that a FP QW semiconductor laser can readily exhibit AM or FM ML depending on the structural and operational conditions.

The first key quantity that prescribes ML states is the detuning d [Eq. (13)]. A sufficiently small detuning d is a necessary condition for ML, Eq. (18) and is determined by the linear and nonlinear dispersions among the relevant modes [Eq. (13)]. Because the linear dispersion causes generally different phase shifts to each of the three modes, there should be, for the laser to operate stably, large nonlinear dispersion that can cancel out the phase difference due to linear dispersion. The detuning d also takes part in the residual phase difference $\Psi^{(s)}$ that characterizes the ML states. A small d value is a necessary condition for a small phase difference $\Psi^{(s)}$ and, thus, AM ML operation.

$\Psi^{(s)}$ includes another term Ψ_0 that is determined by the nonlinear cross-mode correlation terms through Eqs. (14) and (15). In addition to the condition of $d\rightarrow 0$, $l_c\rightarrow 0$ and $l_s<0$ are required for an ideal AM ML.

The lengths of the cavity and gain region along the cavity axis affect the ML conditions. When the cavity length is short, the mode separation is large, and phase differences between adjacent modes then become large for a given length of the gain region. In this case, large nonlinear effects are required for canceling out the large linear phase difference. This implies that there may be a limit to shortening the cavity length for obtaining AM ML, because there may be a limitation in the optical field intensity obtainable in a short cavity laser. On the other hand, a short cavity is preferable to a long one in order to keep l_c small and l_s negative, i.e., AM ML. The latter can be intuitively understood if we think that, when the gain region is long, the optical modal fields undergo much phase differences within one round trip compared to short gain structures with the same cavity-length. Thus, there may be a cavity-length region where AM ML can be observed. The features are demonstrated in Fig. 2, which reveals the AM ML in FP semiconductor lasers with short cavity lasers and the FM ML with longer cavity lasers.

A criterion $\gamma_c\gamma/\Delta^2$, where Δ is the adjacent-mode separation, can be derived from Eqs. (14) and (15). If the value goes higher, $|l_c|$ tends to increase and l_s tends to turn to be positive. Then FM ML occurs. This is shown in Fig. 2(a)–2(c): If Δ is smaller, $\Psi^{(s)}$ becomes larger. We can see typically in Fig. 2(b) that $\Psi^{(s)}$ increases as $\gamma_c(=B\sqrt{n_{2D}p_{2D}})$ increases.

We demonstrated in Figs. 2(c) and 2(d) that if FM ML occurs for a cavity length, it can turn to AM ML by restricting the gain region to a half part of the middle of the cavity. This can be predicted from the fact that the sign of $S^z_{n\mu\rho\sigma}$ in Eq. (5) and, hence, l_s can be turned to the opposite by configuring $S^z(z)$ independently of the internal optical and electronic state of the laser.

The QW structure is related to ML features through the confinement factor. The confinement factor scales the amount of interaction between optical fields and QW's as the optical media. If the confinement factor is too small, the amplitude may not reach enough values to generate high nonlinear effects that are able to cancel out the linear dispersion. For example, there was no stable solution for a single QW laser with a 300-μm-cavity length in the range of 0.8–1.2 V. Simulations also show that, if the confinement factor is too high, the dynamical variables of the laser tend to fluctuate and the laser does not exhibit stable ML.

The well width affects the oscillating frequency because subband energies are related to the well width. For example, the center-mode energy for a 300-μm-cavity laser is 0.798 eV for a 6-nm well, while being 0.802 eV for a 5.3-nm well, as has been seen in Sec. II B. The center-mode energy is rather sensitive to the well width. Further, a wide well can facilitate the settling of the 600-μm-cavity laser into the AM

ML state, as shown in Figs. 2(b) and 3.

Throughout this paper, we have considered a shallow QW structure that can hold a single subband only in the conduction band. Consequently, electrons distribute in broad spectral ranges compared with cases of multiple subbands. The broad energy spectrum of an electron distribution benefits the homogeneously broadened gain required for achieving multimode operation.

Spectral ranges of the operating modes of a semiconductor laser can be calculated by the present laser model within the decoupled approximation, as shown in Figs. 2 and 3. However, the actual spectral widths of the lasers are narrower than those of the calculated ones, as shown in Fig. 6. The discrepancies can be ascribed to the inadequacy of the decoupled approximation for the case of broad gain spectra as treated in this paper. For cases of whole area excitation in FP cavities, actual amplitudes on the lower-energy side of the calculated center-mode energy are weaker than calculated ones because of lower gains. It is plausible that the stable condition is actually broken up rather rapidly on the lower-energy side as compared to the calculated results by "decoupled approximation."

Experimentally, we observed well-defined mode-locked pulses from 300- to 600-μm-cavity lasers. When the injection-current density was increased, extinction ratios of the ML pulses were increased and the temporal pulse width was reduced. This reveals that the spectral range of locked modes is broadened by the increased carrier density in the QW, and that all modes are correlated with each other. The experimentally obtained features of the ML of QW semiconductor lasers are substantially consistent with the present model as described above.

Although we have treated rather specific semiconductor lasers, we believe that the results presented in this paper reveal essential features of multimode operation of semiconductor lasers and elucidate passive ML operations of FP semiconductor lasers.

APPENDIX A: RATE EQUATIONS FOR DIAGONAL ELEMENTS OF THE DENSITY MATRIX

The elements of the density matrix for an electron interacting with the optical field in the semiconductor QW may obey the following equations [13]:

$$\frac{\partial \rho_{cc\mathbf{k}}}{\partial t} = \xi_{c\mathbf{k}} - \gamma_{c\mathbf{k}}\rho_{cc\mathbf{k}} + \imath\hbar^{-1}\mathcal{E}(t)(d_{cv\mathbf{k}}\rho_{vc\mathbf{k}} - d_{vc\mathbf{k}}\rho_{cv\mathbf{k}}), \tag{A1}$$

$$\frac{\partial \rho_{vv\mathbf{k}}}{\partial t} = \xi_{v\mathbf{k}} - \gamma_{v\mathbf{k}}\rho_{vv\mathbf{k}} - \imath\hbar^{-1}\mathcal{E}(t)(d_{cv\mathbf{k}}\rho_{vc\mathbf{k}} - d_{vc\mathbf{k}}\rho_{cv\mathbf{k}}), \tag{A2}$$

and

$$\frac{\partial \rho_{cv\mathbf{k}}}{\partial t} = -(\gamma + \imath\omega_{\mathbf{k}})\rho_{cv\mathbf{k}} - \imath\hbar^{-1}\mathcal{E}(t)d_{cv\mathbf{k}}(\rho_{cc\mathbf{k}} - \rho_{vv\mathbf{k}}), \tag{A3}$$

where $\rho_{\lambda\lambda'\mathbf{k}}$ ($\lambda,\lambda'=c$ or v) are elements of the density matrix, subscript $c(v)$ denotes the conduction (valence) band, $\xi_{c\mathbf{k}}$ ($\xi_{v\mathbf{k}}$) is the pumping rate to the state $\mathbf{k}$ in the conduction (valence) band, and $\gamma_{c\mathbf{k}}$ ($\gamma_{v\mathbf{k}}$) is the decay rate of the state $\mathbf{k}$ through spontaneous emission. In Eq. (A3), we write

$$\gamma = \frac{1}{2}(\gamma_{c\mathbf{k}} + \gamma_{v\mathbf{k}}) + \gamma_{ph}, \tag{A4}$$

where γ_{ph} is the dipole-dephasing rate. Here, we ignore the $\mathbf{k}$ dependence of the decay rates. As a matter of fact, γ_{ph} dominates the value of γ and we assume that γ_{ph} has a constant value. In Eq. (A3), the transition energy $\hbar\omega_{\mathbf{k}}$ is given by

$$\hbar\omega_{\mathbf{k}} = \hbar\omega_{c\mathbf{k}} + \hbar\omega_{v\mathbf{k}} + E_G,$$

where E_G is the band-gap energy at $\mathbf{k}=0$, and the electron and hole energies are given by

$$\hbar\omega_{c\mathbf{k}} = E_i^c + \frac{\hbar^2}{2m_c}\mathbf{k}^2$$

and

$$\hbar\omega_{v\mathbf{k}} = E_j^v + \frac{\hbar^2}{2m_v}\mathbf{k}^2,$$

where E_i^c (E_j^v) is the ith (jth) subband energy in the conduction (valence) band in the QW and m_c and m_v are effective masses of electrons and holes, respectively.

Equations (A1)–(A3) describe interband kinetics of the free-carrier system. We solve these equations in a simplified situation. First, we treat $\mathcal{E}$ as a perturbation and solve the equations to the third order of $\mathcal{E}$. Second, excited free electrons in the conduction band and holes in the valence band are thermally in quasiequilibrium. Third, the electronic and optical state in the cavity is assumed to be in a steady state, and thus the carrier distribution and the amplitudes of optical fields can be seen to be constant within the spontaneous recombination time $1/\gamma_{c\mathbf{k}}$. Further, we ignore free-carrier-decay processes due to nonradiative recombinations, because nonradiative-recombination centers are saturated when the QW is highly excited, as in the case of lasers in operation, and the spontaneous-emission process dominates the decay rate. Particularly, this is the case for $InP/In_{1-x}Ga_xAs_yP_{1-y}$-based semiconductor lasers.

If the optical field is absent in the cavity, the formal solution of Eq. (A1) is obtained as $\rho_{cc\mathbf{k}}^{(0)} = \xi_{c\mathbf{k}}\gamma_{c\mathbf{k}}^{-1}$ and is equal to the Fermi-Dirac distribution

$$\rho_{cc\mathbf{k}}^{(0)} = \frac{1}{\exp\{(\hbar\omega_{c\mathbf{k}} - \mu_c)/kT\} + 1}, \tag{A5}$$

where k is Boltzmann's constant, T is the absolute temperature, and μ_c is the quasi-Fermi energy in the conduction band for the quasiequilibrium state, and is determined so that the 2D electron density n_{2D} is given by

$$n_{2D}=\frac{1}{V}\sum_{\mathbf{k}}\frac{1}{\exp\{(\hbar\omega_{c\mathbf{k}}-\mu_c)/kT\}+1}. \tag{A6}$$

Similarly, defining the 2D hole density p_{2D} and the quasi-Fermi energy in the valence band by

$$p_{2D}=\frac{1}{V}\sum_{\mathbf{k}}\frac{1}{\exp\{(\hbar\omega_{v\mathbf{k}}-\mu_v)/kT\}+1}, \tag{A7}$$

we obtain the lowest-order solution of Eq. (A2) as

$$\rho^{(0)}_{vv\mathbf{k}}=1-\frac{1}{\exp\{(\hbar\omega_{v\mathbf{k}}-\mu_v)/kT\}+1}. \tag{A8}$$

The first-order solution of Eq. (A3) is obtained under the rotating-wave approximation by substituting $\mathcal{N}_{\mathbf{k}}\equiv(\rho^{(0)}_{cc\mathbf{k}}-\rho^{(0)}_{vv\mathbf{k}})$ for $(\rho_{cc\mathbf{k}}-\rho_{vv\mathbf{k}})$ in Eq. (A3) as

$$\rho^{(1)}_{cv\mathbf{k}}=-\frac{1}{2}\imath\hbar^{-1}d_{cv\mathbf{k}}\mathcal{N}_{\mathbf{k}}(y,z)\sum_{\sigma}E_{\sigma}(t)\times\exp\{-\imath(\nu_{\sigma}t+\phi_{\sigma})\}Y_{\sigma}(y)Z_{\sigma}(z)\mathcal{D}(\omega_{\mathbf{k}}-\nu_{\sigma}). \tag{A9}$$

Substituting Eq. (A9) into Eq. (A1), we have

$$\frac{\partial\rho_{cc\mathbf{k}}}{\partial t}=\xi_{c\mathbf{k}}-\gamma_{c\mathbf{k}}\rho_{cc\mathbf{k}}-\frac{1}{4}\left(\frac{d_{cv\mathbf{k}}}{\hbar}\right)^2\mathcal{N}_{\mathbf{k}}(y,z)\times\sum_{\rho}\sum_{\sigma}E_{\rho}E_{\sigma}Y_{\rho}Y_{\sigma}Z_{\rho}Z_{\sigma}\mathcal{D}(\omega_{\mathbf{k}}-\nu_{\sigma})\times\exp[\imath\{(\nu_{\rho}-\nu_{\sigma})t+\phi_{\rho}-\phi_{\sigma}\}]+\text{c.c}, \tag{A10}$$

where we use the relations,

$$\rho_{cv\mathbf{k}}=\rho^{*}_{vc\mathbf{k}},$$

$$d_{cv}=d^{*}_{vc}.$$

By summing up over $\mathbf{k}$ space, spatially averaging Eq. (A10) and using Eq. (A6), Eq. (A10) leads to Eq. (6).

APPENDIX B: MATRIX ELEMENT OF DIPOLE MOMENT

The matrix element of the electric dipole is given by

$$|(d_{cv\mathbf{k}})_{ij}|^2=\left(\frac{e}{m_0\omega_{\mathbf{k}}}\right)^2M^2A^{v}_{ij}C^{v}_{ij}, \tag{B1}$$

where e denotes the elementary charge, m_0 is the rest mass of an electron, and, by using the Kane's model [19],

$$M^2=\frac{m_0^2E_G(E_G+\Delta_s)}{2m_c\left(E_G+\frac{2}{3}\Delta_s\right)},$$

with the spin-orbit splitting Δ_s. In Eq. (B1), C^{v}_{ij} is the overlap integral of the envelope functions, ψ_{ci}, ψ_{vj}, of the 2D electrons and holes for the ith and jth sublevels, respectively. A^{v}_{ij} is given for TE polarization by

$$A^{v}_{ij}=\begin{cases}\frac{1}{2}(1+\cos^2\theta^{v}_{ij}) & \text{for } v \text{ being a heavy hole}\\ \frac{1}{3}\left\{\frac{1}{2}(1+\cos^2\theta^{v}_{ij})+2\sin^2\theta^{v}_{ij}\right\} & \text{for } v \text{ being a light hole,}\end{cases}$$

where

$$\cos^2\theta^{v}_{ij}=\frac{E^2_{ci}}{E^2_{ci}+(Q^{v}_{ij})^2},$$

$$Q^{v}_{ij}=\frac{\hbar^2\mathbf{k}^2}{2}\left(\frac{1}{m_c}+\frac{1}{m_v}\right).$$

[1] See, for instance, S. Arahira, Y. Matsui, and Y. Ogawa, IEEE J. Quantum Electron. **32**, 1211 (1996), and references therein.
[2] J.P. Van der Ziel, in *Semiconductor Semimetals*, edited by W. T. Tsang (Academic Press, New York, 1985), Vol. 22, Pt. B.
[3] A.E. Siegman, *Lasers* (University Science Books, California, 1986).
[4] A. Yariv, *Quantum Electronics*, 3rd ed. (Wiley, New York, 1989).
[5] H.A. Haus, IEEE J. Sel. Top. Quantum Electron. **6**, 1173 (2000).

[6] M. Sargent, III, M. O. Scully, and W. E. Lamb, Jr., *Laser Physics* (Addison-Wesley, Tokyo, 1974).
[7] W.E. Lamb, Jr., Phys. Rev. **134**, A1429 (1964).
[8] W. W. Chow, S.W. Koch, and M. Sargent, III, *Semiconductor-Laser Physics* (Springer-Verlag, Berlin, 1994).
[9] H. Ito, H. Yokoyama, S. Murata, and H. Inaba, Electron. Lett. **15**, 738 (1979).
[10] Y. Tsuchiya, M. Miwa, and M. Koishi, Appl. Phys. Lett. **53**, 6671 (1982).
[11] In Ref. [6], the terms ''amplitude modulation (AM)'' and ''frequency modulation (FM)'' denote the two steady-state solutions of the coupled-mode equations in the context of mode-locked three-mode operation of lasers. In AM ML, all the modes are in-phase, i.e., the residual phase difference $\Psi^{(s)}$ of one from the other two modes is zero and in FM ML $\Psi^{(s)}=\pi$. In this paper, we denote AM ML for $-\pi/2<\Psi^{(s)}<\pi/2$ and FM ML for $\pi/2<\Psi^{(s)}<3\pi/2$ because, in semiconductor lasers, the $\Psi^{(s)}$ value is not restricted to zero or π.
[12] A part of the experimental results was presented in the following meeting and workshop: Y. Nomura *et al.*, IEICE Technical Report No. LQE99-8, 1999 (unpublished); in Abstracts in The 6th International Workshop on Femtosecond Technology, Chiba, 1999 (unpublished).
[13] H. Haug and S. W. Koch, *Quantum Theory of the Optical and Electronic Properties of Semiconductors*, 3rd ed. (World Scientific, New Jersey, 1998).
[14] We derived the equations following Refs. [6,13]. See also Ref. [8].
[15] C. M. Snowden, *Introduction to Semiconductor Device Modeling* (World Scientific, Singapore, 1986).
[16] See Table 3.1 of G.P. Agrawal and N.K. Dutta, *Long-Wavelength Semiconductor Lasers* (Van Norstrand Reinhold, New York, 1986).
[17] W.W. Chow, A. Knorr, S. Hughes, A. Girndt, and S.W. Koch, IEEE J. Sel. Top. Quantum Electron. **3**, 136 (1997).
[18] E. Winter and E.P. Ippen, Appl. Phys. Lett. **44**, 999 (1984).
[19] E.O. Kane, J. Phys. Chem. Solids **1**, 249 (1957).